Integrated time-lapse geoelectrical imaging of wetland hydrological processes

S.S. Uhlemann[1,2,*], J.P.R. Sorensen[3], A.R. House[4], P.B. Wilkinson[1], C. Roberts[4], D.C. Gooddy[3], A.M. Binley[5], J.E. Chambers[1]

1 – Geophysical Tomography Team, British Geological Survey, Nottingham, UK

2 – ETH-Swiss Federal Institute of Technology, Institute of Geophysics, Zurich, Switzerland

3 – Groundwater Processes Team, British Geological Survey, Wallingford, UK

4 – Centre for Ecology and Hydrology, Wallingford, UK

5 – Lancaster Environment Centre, Lancaster University, Lancaster, UK

* Corresponding author: Sebastian Uhlemann, suhl@bgs.ac.uk

Key Points

- Characterization of wetland hydrological processes by resistivity monitoring
- Highlight seasonally dependent, layered groundwater system
- Quantification of peat shrink-swell by edge detection applied to ERI data

Abstract

Wetlands provide crucial habitats, are critical in the global carbon cycle, and act as key biogeochemical and hydrological buffers. The effectiveness of these services is mainly controlled by hydrological processes, which can be highly variable both spatially and temporally due to structural complexity and seasonality. Spatial analysis of 2D geoelectrical monitoring data integrated into the interpretation of conventional hydrological data has been implemented to provide a detailed understanding of hydrological processes in a riparian wetland. This study shows that a combination of processes can define the resistivity signature of the shallow subsurface, highlighting the seasonality of these processes and its corresponding effect on the wetland hydrology. Groundwater exchange between peat and the underlying river terrace deposits, spatially and temporally defined by geoelectrical imaging and verified by point sensor data, highlighted the groundwater dependent nature of the wetland. A 30 % increase in peat resistivity was shown to be caused by a nearly entire exchange of the saturating groundwater. For the first time, we showed that automated interpretation of geoelectrical data can be used to quantify shrink-swell of expandable soils, affecting hydrological parameters, such as, porosity, water storage capacity, and permeability. This study shows that an integrated interpretation of hydrological and geophysical data can significantly improve the understanding of wetland hydrological processes. Potentially, this approach can provide the basis for the evaluation of ecosystem services and may aid in the optimization of wetland management strategies.

Index terms

1835 Hydrogeophysics, 1890 Wetlands, 1830 Groundwater/surface water interaction, 0483 Riparian systems

Key words

Wetland; resistivity monitoring; shrink-swell; layered groundwater system

1. Introduction

Groundwater-dependent ecosystems (GDEs) are priority habitats under the European Habitats Directive [*EEC*, 1992]. Wetlands form one of the main GDE typologies and, in addition to their habitat provision, are notable for their critical contribution to the global carbon cycle [*Bridgham et al.*, 2013; *Mitsch et al.*, 2013]. For example, wetlands account for 20-25% of organic carbon in soils [*Gorham*, 1995], contribute 20-40% of current global methane emissions [*Bloom et al.*, 2010], and explain 70% of annual variations in atmospheric methane concentrations [*Bridgham et al.*, 2013]. The main drivers regulating wetland carbon cycles are related to hydrological factors such as water movement [*Limpens et al.*, 2008]. These factors are also a key control for the establishment, maintenance and restoration of wetland habitats [*Mitsch and Gosselink*, 2007]: impacting both vegetation [*Baldwin et al.*, 2001; *House et al.*, 2015] and fauna [*Ausden et al.*, 2001; *McMenamin et al.*, 2008].

In addition to their impact on carbon cycles, riparian wetlands also act as key biogeochemical and hydrological buffers [*Mitsch*, 1992; *Gilliam*, 1994; *Mitsch and Gosselink*, 2007]. They can provide a nitrate and carbon sink, thus increase water quality, and may act as flood defenses [*Theriot et al.*, 2013; *Martinez-Martinez et al.*, 2014]. However, around 55% of total wetland area has been lost in the last century [*Davidson*, 2014] and there are now national and international initiatives to encourage their restoration.

Hydrological processes in wetlands can be highly spatially and temporally dependent, as a result of heterogeneity in the subsurface [*Holden and Burt*, 2002; *House et al.*, 2015]. There is also ongoing uncertainty regarding water movement within peat-dominated wetlands [*Reeve et al.*, 2000, 2006]. Seasonal changes in moisture content are known to result in changes in peat volume with moisture loss causing peat compaction and moisture gain peat expansion. These volumetric changes directly

affect the hydraulic properties of peat causing changes in hydraulic conductivity, porosity, and water storage capability [*Price and Schlotzhauer*, 1999; *Kennedy and Price*, 2005]. For example, peat shrinkage has been demonstrated to reduce hydraulic conductivity by up to three orders of magnitude and therefore aiding as a self-preservation mechanism against further moisture loss [*Chow et al.*, 1992; *Price*, 2003]. Thus, an understanding of peat shrink and swell is essential to accurately model hydraulic processes in peat-dominated wetland.

Investigations of subsurface hydrological properties and processes in wetlands are typically restricted to a limited number of piezometers [*Bradley*, 1997; *Kehew et al.*, 1998]. This is a result of wetland inaccessibility due to ecological sensitivity, their frequent inundation, as well as the high costs of drilling. Geophysical methods can noninvasively and cost-effectively achieve high spatial coverage to improve our hydrological understanding in these heterogeneous settings [*Kettridge et al.*, 2008; *Lowry et al.*, 2009; *Comas et al.*, 2011; *Chambers et al.*, 2014b].

Electrical resistivity imaging (ERI) is a well-developed method for volumetric imaging of temporal hydrological processes [*Cardenas and Markowski*, 2011; *Musgrave and Binley*, 2011; *Binley et al.*, 2015], as the resistivities of earth materials are sensitive to changes in moisture content, temperature and pore water chemistry. The resistivity distribution of the subsurface is determined based on the measurement of electrical potentials at discrete locations along the surface or in boreholes caused by the application of electrical currents. Geophysical techniques targeting electrical (and dielectrical) subsurface properties, such as ground penetrating radar, and electromagnetic and geoelectrical methods, are commonly used to investigate subsurface structures in wetlands, allowing for identification of hydrological properties and processes [*Comas et al.*, 2004; *Kettridge et al.*, 2008]. Monitoring studies aiming to image time varying wetland processes are more rarely applied. ERI monitoring has been used to reveal temperature dynamics in a wetland environment indicating groundwater recharge [*Musgrave and Binley*, 2011], and to image methanogenesis in peat blocks [*Slater et al.*, 2007] by exploiting the resistivity contrast caused by

seasonal entrapment of non-conductive gas within the originally saturated and conductive pore space. Laboratory studies on the electrical properties of peat have also showed that its bulk resistivity is highly sensitive to changes in pore water resistivity [*Comas and Slater*, 2004; *Ponziani et al.*, 2012].

In recent years, automated interpretation of resistivity models has been developed [*Chambers et al.*, 2012, 2014b, 2015; *Audebert et al.*, 2014; *Ward et al.*, 2014] and applied to extract interfaces of lithological boundaries or other target features from 2D/3D resistivity images. It has been shown that the accuracy of such methods can be comparable to shallow intrusive investigations, such as sonic or shell-and-auger drilling [*Chambers et al.*, 2012, 2014b], when estimating depth-to-bedrock. Applying these methods to time-lapse imagery could potentially identify movement within any target interface. Expansive soils, such as peat, are subject to large volume changes. Therefore, as distances from the surface to lithological boundaries change due to electrodes moving with the soil, automated ERI interface detection could identify seasonal shrink-swell during annual drying-wetting phases.

The aim of this study is to apply time-lapse geoelectrical imaging integrated with hydrological and environmental sensor data to improve the understanding of wetland functioning as a regulator of both carbon cycling and habitat provision. In particular, this research is focused on the imaging of hydrological processes affecting the resistivity signature of near-surface pore waters, and potential upwelling of nutrient rich, deeper waters into shallow peat layers. Detecting seasonal changes in peat volume from ERI data will also aid in supporting future studies on hydrologic process modelling without the need for additional monitoring of surface movements, by providing information on the temporal characteristics of water storage capacities and hydraulic conductivities. Integrating geoeletrical and conventional hydrological data allows to study spatially complex processes, which are not able to be captured employing point sensor data only.

2. Methodology

2.1. Study Area

The study area is a 10 ha riparian wetland on the River Lambourn, in Boxford, Berkshire, UK (Figure 1a). It is designated as a Special Site of Scientific Interest (SSSI) owing to the habitat it provides for the near-threatened Desmoulin's whorl snail [*Killeen*, 2003]. The River Lambourn drains the Chalk of the Berkshire Downs and is strongly groundwater dependent with a base flow index of 0.96 at the nearest gauging station at Shaw [*Marsh and Hannaford*, 2008]. It has a near-natural flow regime and good water quality, thus providing a reference observatory against which to compare other more anthropogenically impacted sites.

The wetland is located 13 km downstream of the ephemeral river head. The underlying bedrock is the Cretaceous Seaford Chalk Formation, a fine-grained white limestone with many flint nodules. However, much of the upper part of the profile has been weathered into a low permeability structureless 'putty' chalk, which is considered to confine the aquifer where present [*House et al.*, 2015]. The irregular surface of the Chalk is overlain by river terrace deposits that are primarily coarse-grained gravels that display a clear braided structure [*Chambers et al.*, 2014b]. In the basal 1-2 m of the gravels, re-worked chalk can be present occluding the available porosity and potentially permeability [*Allen et al.*, 2010]. Water movement within the saturated zone is thus predominantly controlled by the numerous vertical and horizontal discontinuities in the chalk and overlying gravels. These gravels are, in turn, overlain by Holocene alluvium (typically < 1 m) comprising predominantly peat, with the thickest deposits occupying a channel-like structure through the site upon a topographic low on the gravels surface (Figure 1b, *Chambers et al., 2014b*). Heterogeneity within the alluvium partly reflects climatic change and anthropogenic impacts, such as large-scale deforestation within the catchment, which are frequently observed in Holocene floodplain sediments [*Newell et al.*, 2015]. Notably, there is an intermittent layer of 0.1-0.2 m of chalky clay within the predominantly peat profile.

The wetland is divided into a northern and southern meadow by the Westbrook Channel, which diverts water from the Lambourn, and through the site, before re-joining the river (Figure 1a). A spring-fed channel also flows south-westwards along the western margins of the southern meadow. Consequently the wetland is almost entirely encircled by surface waters. These exert a strong control on the water table across the wetland. Increases and rapid reductions in channel stage caused by seasonal weed growth and cutting (to increase river flow conveyance), respectively, results in near equivalent changes in the peat water table [*Old et al.*, 2014]. Nevertheless, the site is considered groundwater dependent, with upwelling water from the Chalk thought to be focused within discrete relic channels in the peat, particularly in the northern meadow. These discharges increase the floral biodiversity of the site through their provision of high nitrate, low phosphate waters, in a wetland dominated by poor fen communities. Away from the localized upwelling, there is strong evidence for nitrate removal through reductive bacterial processes [*House et al.*, 2015].

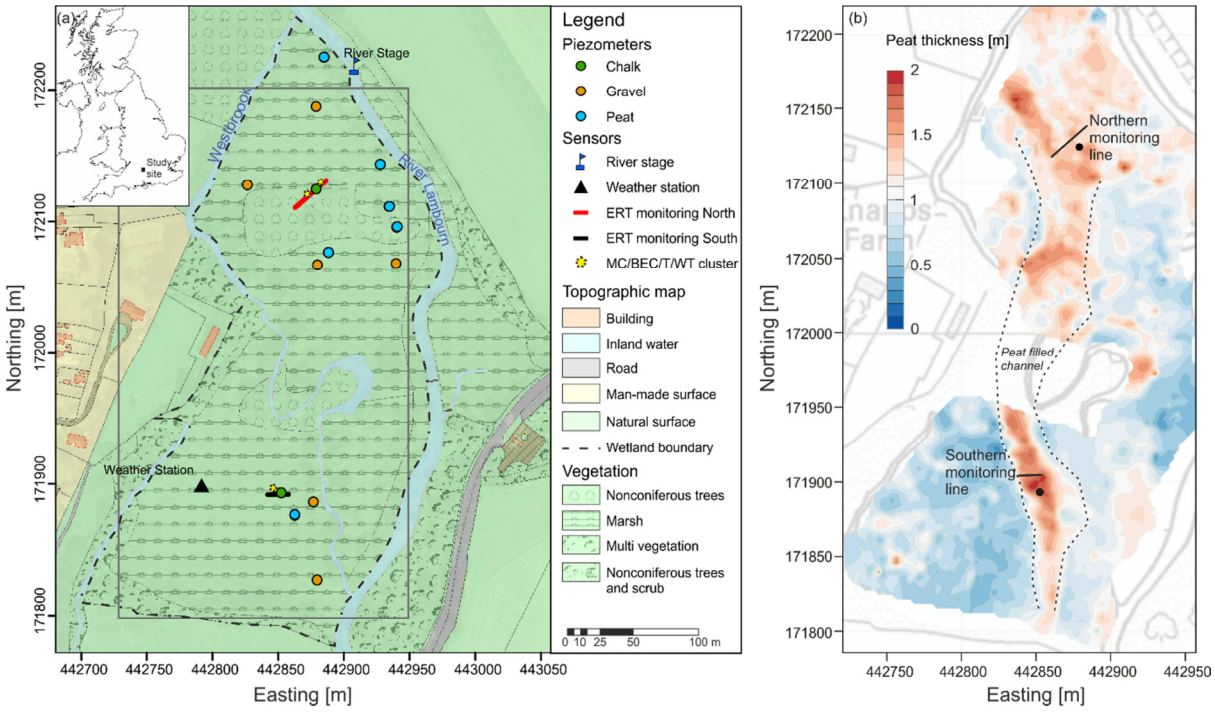

Figure 1 a) Map of the River Lambourn Observatory and the instrumentation network. Inset shows the location of the observatory in the UK. MC – Moisture content, BEC – Bulk Electrical Conductivity, T – Temperature, WT – Water table. Grey box outlines area of b), which shows the ERI monitoring locations superimposed on a map of intrusively determined peat

thicknesses (modified from Chambers et al. [2014b]). a) and b) are plotted on an Ordnance Survey base layer (© Crown copyright and database rights 2015 Ordnance Survey 100021290).

2.2. ERI monitoring installation

In a previous study, Chambers et al. [2014b] employed 3D geoelectrical imaging and interface detection methods to reconstruct the deposit architecture of the Lambourn observatory. They imaged the spatial variability of peat thickness, revealing a channel of thick peat deposits crossing the wetland, and correlated the data with intrusive peat thickness estimates (Figure 1b). Within the underlying gravels, structural features characteristic of braided fluvial systems were found. This study focusses on time-lapse 2D ERI to characterize dynamic hydrological processes within the wetland.

Two geoelectrical monitoring arrays were installed in each meadow of the wetland during December 2012 (Figure 1). The locations targeted thicker peat deposits (>1 m), including a channel-structure identified by intrusive peat thickness measurements (Figure 1b) and 3D ERI surveying in the southern meadow.

An electrode spacing of 0.5 m was chosen to provide sufficient lateral and vertical resolution to image hydrological processes in the highly heterogeneous wetland material. This spacing enabled imaging of the resistivity distribution (with final model cell areas ranging between 0.035 m^2 and 0.145 m^2) to a depth of up to 1.5 m below the peat-gravel interface, which can be found between 1.0 and 1.5 m below ground level (bgl). The northern and southern arrays comprised 64 stainless-steel electrodes (31.5 m in length) and 32 stainless-steel electrodes (15.5 m in length), respectively, permanently installed just below the surface. The northern array was greater in length to traverse two relic channels within the peat that were considered to be areas of groundwater upwelling [*House et al.*, 2015], whilst the southern array targeted a single relic channel-structure containing the thickest peat deposits [*Chambers et al.*, 2014b].

A dipole-dipole type measurement configuration was chosen with dipole lengths (a) of 0.5 m, 1.0 m, 1.5 m, and 2.0 m, and dipole separations (n) of 1a to 8a. The dipole-dipole measurement configuration was chosen, as it provides good resolution of both vertical and horizontal resistivity changes [*Chambers et al.*, 2002; *Dahlin and Zhou*, 2004]. Calculating the depth of investigation (DOI) index [*Oldenburg and Li*, 1999] shows high sensitivity throughout the imaging section with DOI indices $R < 0.3$. Employing a cut-off value of $R = 0.05$ indicated the effective depths of investigation to be ~3 m and ~2 m for the northern and southern array, respectively. The peat-gravel interface is at a depth where it can be expected to be well-resolved by the longer northern array, but is likely to be less well resolved by the southern array, partly because the interface is at a greater depth and partly because the southern array is shorter. ERI monitoring commenced in December 2012, and was followed by monthly data acquisition from March 2013, resulting in 21 data sets over a 24 month period.

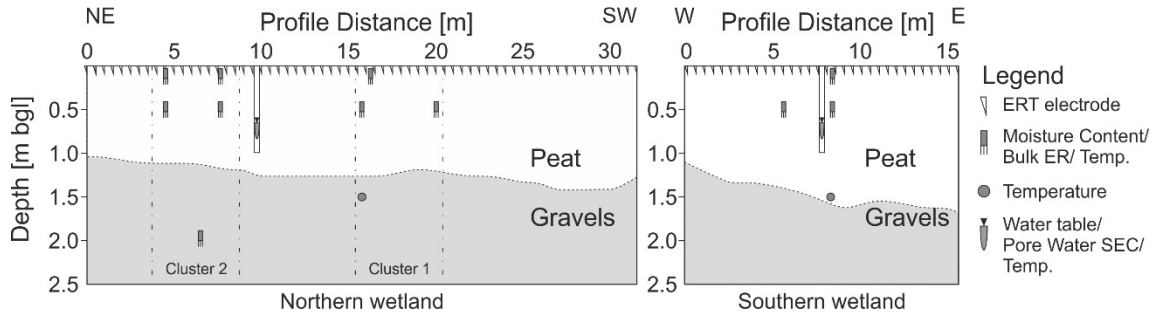

Figure 2 Schematic of the ERI arrays and sensor installations for the northern and southern meadows. Note that the DOI index of the northern and southern installation was R = 0.05 at about 3 m and 2 m depth, respectively, defining the effective depth of investigation.

To obtain a model of the subsurface resistivity distribution, the measured data needs to be inverted. ERI inversion is fundamentally a non-unique process (in that an infinite number of models fit the data equally well; e.g., *Olayinka and Yaramanci* [2000]), so smoothness constraints are applied to define an optimal solution in terms of a smoothly varying resistivity model. Hence, additional subsurface data are needed to inform the ERI inversion and to compare the resulting models, thereby ensuring their reliability [e.g. *Kuras et al.*, 2009; *Wagner et al.*, 2013; *Gunn et al.*, 2014;

202 *Hermans et al.*, 2015]. For this purpose, environmental sensors measuring moisture content (MC),
203 bulk electrical resistivity (BER), temperature, and water table (WT) were installed at different
204 locations and depths along the monitoring transects (Figure 2).

205 In the northern meadow, clusters of sensors were installed in two separate phases. The first cluster
206 was installed with the ERI array in December 2012. This comprised MC, BER (corrected for
207 temperature effects; sampling volume ~$2.75*10^{-4}$ m^3), and temperature sensors at 0.1 m and 0.5 m
208 depth, and an additional temperature sensor at 1.5 m depth (Figure 2). The second cluster was
209 established in December 2013, with MC, BER, and temperature sensors installed at 0.1 m, 0.5 m, and
210 2 m below ground level, where the deepest sensor was within the gravels. These additional sensors
211 were installed after a preliminary analyses of the ERI monitoring data [*Uhlemann et al.*, 2014]. In the
212 southern meadow, the sensor installation was similar to the first phase in the northern part and
213 installed in December 2012. In both the northern and southern wetland a piezometer adjacent to
214 the array was equipped with instrumentation recording water level (assumed equivalent to hydraulic
215 head), temperature, and pore water electrical conductivity in April 2013. All sensors were logged at
216 30-minute intervals.

217 ## 2.3. Resistivity data error

218 For data quality control, every ERI dataset was recorded employing a full set of reciprocal
219 measurements, comprising 1528 and 516 measurement pairs for the northern and southern
220 meadows, respectively. The reciprocity theorem states that interchanging current injection and
221 potential dipole (i.e. normal and reciprocal measurement) should result in the same data. Hence,
222 any difference between the two measurements can be used as a robust estimate of the data error
223 [*LaBrecque et al.*, 1996].

224 These reciprocal errors were calculated for each dataset, creating a time-series of error distributions
225 over the monitoring period (Figure 3). Reciprocal errors were also processed and analyzed as

outlined in Koestel et al. [2008] in order to develop an error model. This model represents the error comprising an absolute measurement error component $a_{N/R}$ and a relative measurement error component $b_{N/R}$ applied to $R_{N/R}$ the mean of the measured normal and reciprocal resistance value. Thus, the reciprocal error can be approximated by:

$$\varepsilon_{N/R} = a_{N/R} + b_{N/R}\left|R_{N/R}\right| \quad (1)$$

Considering the complete time series, the data of the northern meadow show very good quality with only about 8% having reciprocal errors above 10%. The smallest errors were recorded before a drop in water table in August 2013 (< 5% of data with errors > 10%), after which errors increased (10% - 50% of data with errors > 10%) despite water table recovery and larger variability. A system malfunction in July and August 2013 could be identified by $a_{N/R}$ exceeding a threshold of 10^{-3} Ω and comparably high values for $b_{N/R}$. Except for these outliers, $a_{n/R}$ and $b_{N/R}$ show significantly less variation then the reciprocal error threshold and are comparable at both meadows.

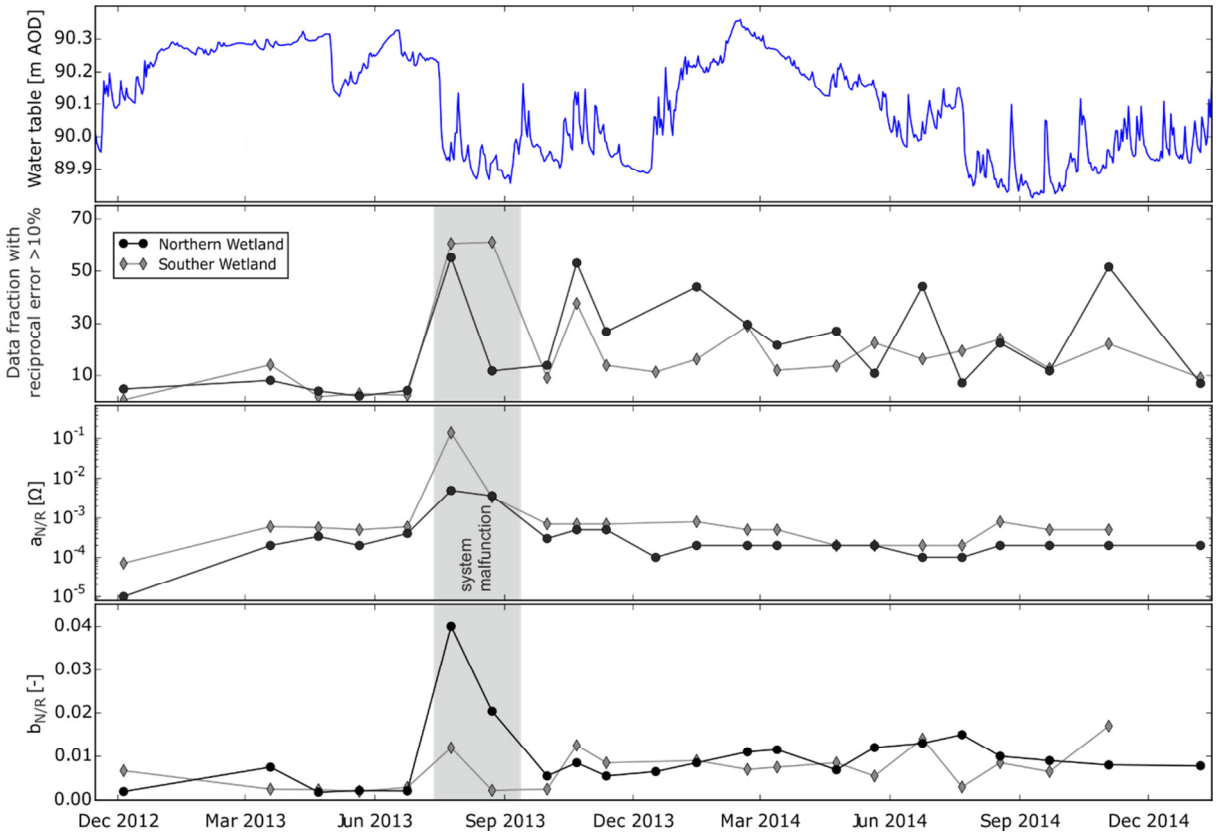

Figure 3 Data error characteristics and water table of the northern meadow. Given are the measured fraction of the data having a reciprocal error above 10 %, as well as the parameters $a_{N/R}$ and $b_{N/R}$ of the error model introduced by Koestel et al. [2008].

Before inversion, data with reciprocal errors exceeding a threshold of 10% were removed from the dataset and replaced by values derived from their respective time-series, using an inverse distance weighting interpolation. This step was necessary, as the employed time-lapse inversion routine requires each measurement set to comprise the same dipole-dipole measurements. Note that data from July and August 2013 were excluded from the time series due to malfunctioning of the ERI measurement system.

2.4. Data inversion

Data were inverted using a smoothness-constrained least-squares inversion method, with the data defined in a space-time domain, allowing for a simultaneous inversion of the complete data set [*Kim et al.*, 2009]. The inversion employed a L1-norm for the data misfit and a L2-norm for the model

roughness [*Loke and Barker*, 1996], favoring smooth resistivity changes in both space and time. To account for the different resolution capabilities, active constraint balancing has been applied to automatically choose the most appropriate Lagrangian multiplier [*Yi et al.*, 2003]. Data were weighted by their respective measured reciprocal errors, opposed to weighting by the modelled error values, provided the error was above a lower limit of 10 % the average percentage noise level, which is calculated from the error values between the 10 % and 90 % percentiles. This step limits the range of inversion weights calculated from the reciprocal error values [*Loke,* 2015*, personal communication*]. . This was done because, although data weighting by modelled and reciprocal error estimates produced virtually identical resistivity models (Figure S1) in standalone inversion of two test data sets, employing the modelled error showed artifacts in the time-lapse inversion. This is likely to be caused by an underestimation of the data error [*LaBrecque et al.*, 1996].For the interpolated values a high error value of about 3 times the standard deviation was chosen to reduce the influence of these data points on the inversion. The inversion converged after 5 iterations as the root-mean-square (RMS) error between modelled and measured data changed by less than 5 % between the last two iterations. The remaining RMS error was 1.79 % and 2.88 % for the northern and southern meadows respectively, thus highlighting the good agreement between the modelled and observed data. Note that the average data error was 0.23 % and 0.29 %, respectively.

Peat expansion and compaction will lead to vertical movements of the electrodes. Note that in the resistivity inversion the electrode locations, and thus the surface topography, are fixed values; this is a limitation of current inversion algorithms. RTK-GPS measurements showed, however, that the topography changes differently along the line over the monitoring period. These lateral variations were found to be less than 5 cm (i.e. 10% of the electrode spacing). While inline displacements of this magnitude are known to cause artefacts of up to 20% in the resistivity models [Szalai et al., 2008; Wilkinson et al., 2010; Uhlemann et al., 2015], Wilkinson et al. [2015] showed that sensitivities of dipole-dipole measurements to electrode displacements perpendicular to the surface are significantly smaller. As introduced slope angles are also << 10°, the errors introduced by assuming a

277 constant surface elevation should be negligible [Tsourlos et al., 1999]. Topographic information from
278 February and September 2014 (representative for maximum and minimum annual elevation) was
279 used in a numerical modelling exercise, showing that resistivity variations caused by variations in
280 electrode positions are less than 10 % (see Figure S2).

281 ## 2.5. Temperature correction

282 Variations in temperature can have significant effects on geoelectrical monitoring experiments [Rein
283 et al., 2004; Hayley et al., 2007] and resistivity models need to be corrected to a standard
284 temperature to avoid misinterpretation of resistivity data [*Chambers et al.*, 2014a; *Chrétien et al.*,
285 2014]. Therefore, multi-level temperature data, from 0.1, 0.5, and 1.5 m below ground level, were
286 fitted to the following heat equation employing the methodology described in Chambers et al.
287 [2014a]:

288 $$T_{\text{model}}(z,t) = T_{\text{mean}} + \frac{\Delta T}{2}\exp\left(-\frac{z}{d}\right)\sin\left(\frac{2\pi}{365}t + \varphi - \frac{z}{d}\right), \quad (2)$$

289 where T_{mean} is the average air temperature, ΔT the amplitude of the temperature variation, z the
290 depth below ground level, d a characteristic depth by which the amplitude of the temperature
291 variation reduced by 1/e, t the day of the year, and φ a phase offset to ensure that the surface
292 temperature variation is in phase with the air temperature.

293 The resistivity models were subsequently corrected (ρ_{cor}) using the ratio model [*Hayashi*, 2004; *Ma*
294 *et al.*, 2010], which in terms of resistivity can be written as:

$$\rho_{cor} = \rho\left[1 + \frac{c}{100}\left(T_{target} - T_{model}\right)\right] \quad (3)$$

295 All models were corrected to a target temperature of T_{target} = 9.84°C (the annual mean air
296 temperature at the site over the monitoring period), employing a correction factor c of -2.95 °C^{-1}.
297 This value was established in the laboratory by temperature-cycling soil samples under constant

298 moisture content and determining their resistivity. Results thus show the resistivity evolution over
299 time compensated for laterally uniform seasonal temperature variations with depth. Note that non-
300 seasonal temperature effects will still influence the imaged resistivity distribution.

301 ### 2.6. Characterizing shrink-swell

302 The imaging space included a significant change in lithology from low resistivity peat to highly
303 resistive gravels (Figure 2). Assuming that the interface between peat and gravel is fixed in space,
304 only shrinkage or swelling of the peat layer can result in changes of the surface elevation. To test
305 whether it is possible to use ERI to image these changes, the peat thickness of the northern meadow
306 was estimated for every survey using both geoelectrical and real-time kinematic global positioning
307 system (RTK-GPS) measurements. From each resistivity model the boundary between peat and
308 gravel was extracted using a fuzzy *c*-means clustering technique [*Ward et al.*, 2014]. This comprises
309 the characterization of the resistivity probability distribution within each model using kernel density
310 estimation to identify distinct resistivity populations that are representative for the peat and gravel.
311 Two approaches to extract the boundary resistivity value have been tested: (1) calculating the
312 probability distribution and clusters for each time step separately and (2) using the probability
313 distribution and clusters for the data from all time steps. For the first approach the boundary is
314 defined by a different resistivity at each time step; for the second the same resistivity value is used
315 for each time step. These two approaches were employed to investigate the effect of the change in
316 resistivity caused by peat expansion and compaction on the estimate. While during expansion pore
317 volume increases and thus resistivity is likely to decrease, during compaction the peat pore volume
318 reduces and resistivity should increase. Considering the likely variations in peat volume and the
319 sensitivity of resistivity to changes in pore volume, the effect on the resistivity falls below the error
320 levels. To quantify shrink-swell of the peat the surface elevation of the monitoring line was re-
321 surveyed for a subset of site visits using RTK-GPS, with repeated GPS surveys showing a precision of
322 < 3 cm.

2.7. Supporting hydrological data

Supplementary hydraulic head data were available from a network of paired piezometers within the peat and gravels (Figure 1). The River Lambourn stage was continually monitored with a pressure transducer, which was corrected to weekly stage board readings to account for sensor drift [*Sorensen and Butcher*, 2011]. Groundwater samples were regularly collected from peat, gravel, and chalk piezometers following purging and specific electrical conductivity (SEC) determined in the field with a portable meter. Monthly chalk water table data were retrieved away from the site (51°11'56.37"N, 01°45'20.00"W) to represent water table conditions within the aquifer in the Lambourn catchment, which were not impacted by weed cutting and growth in the river [*Old et al.*, 2014].

3. Results

3.1. Hydrology

Water levels conformed to the typical seasonal pattern in the UK: peaking between January and April and reaching the annual minimum between August and November (Figure 4). Rising chalk heads appear to initiate seasonal (Jan-May/June) positive upward vertical head differentials between the gravels and peat within the wetland (Figure 5). These were greatest in early 2014 following exceptional rainfall in Winter 2013/2014 [*Muchan et al.*, 2015], which resulted in unusually high chalk heads. Positive vertical head differentials appear to correlate with a reduction in peat pore water SEC towards that found in the Chalk and gravels. Note that pore water SEC values were measured on water samples taken from piezometers screened acrossed the whole peat profile.

Heads within the peat fluctuated between the ground surface and around 0.3 m bgl. Rapid recessions in peat head in response to river weed cutting and a reduction in stage were evident, e.g. July 2013, May and July 2014, initiating rapid recessions in peat water table (Figure 5).

Changes in MC were less than 0.05 m^3/m^3 in the northern meadow and were concurrent with the peat head dynamics (Figure 4). The BER data from 0.1 m depth show significant increases in the near-surface resistivity following the falling water table in July 2013 and 2014. . Although the water table remained at a constant level between February and June in both 2013 and 2014, near-surface resistivities decreased by more than 80%. The deeper sensors at 0.5m bgl show a linear correlation between resistivity and MC (*Pearson r* = 0.81), despite its inverse nature [*Archie*, 1942]. Thus, in both the near surface and deeper monitoring locations, resistivity dynamics are likely to be dominated by changes in pore water resistivity.

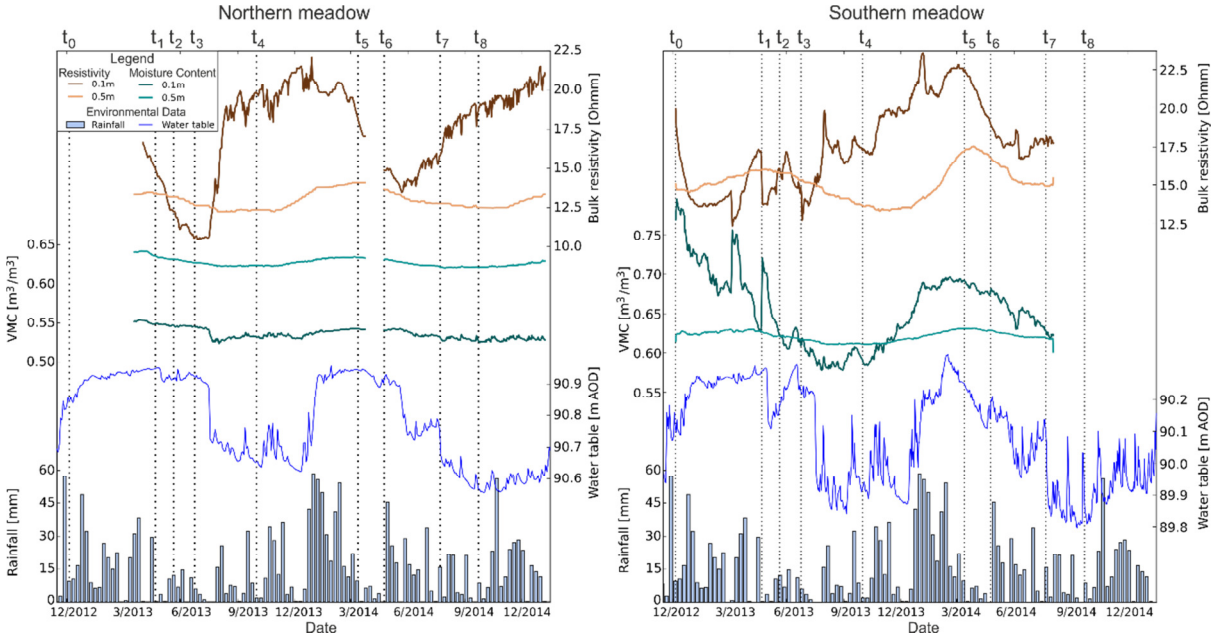

Figure 4 Daily rainfall, peat heads, and multilevel moisture content and bulk resistivity (for 0.5m below ground level the means of the measurements of the two sensors are shown) throughout the ERI monitoring period for the two meadows. MC and resistivity data of the northern meadow was acquired at cluster 1.

In the southern meadow, the more pronounced changes in MC in the near-surface align with the peat heads, but show no response to sudden head changes caused by the weed cuts in the river. The resistivity of the near-surface shows decreasing resistivity during periods of steady, high water table and moisture content (i.e. February 2014 to June 2014), while deeper sensors show increasing resistivity with increasing moisture content (*Pearson r* = 0.78; correlation most pronounced in 2014).

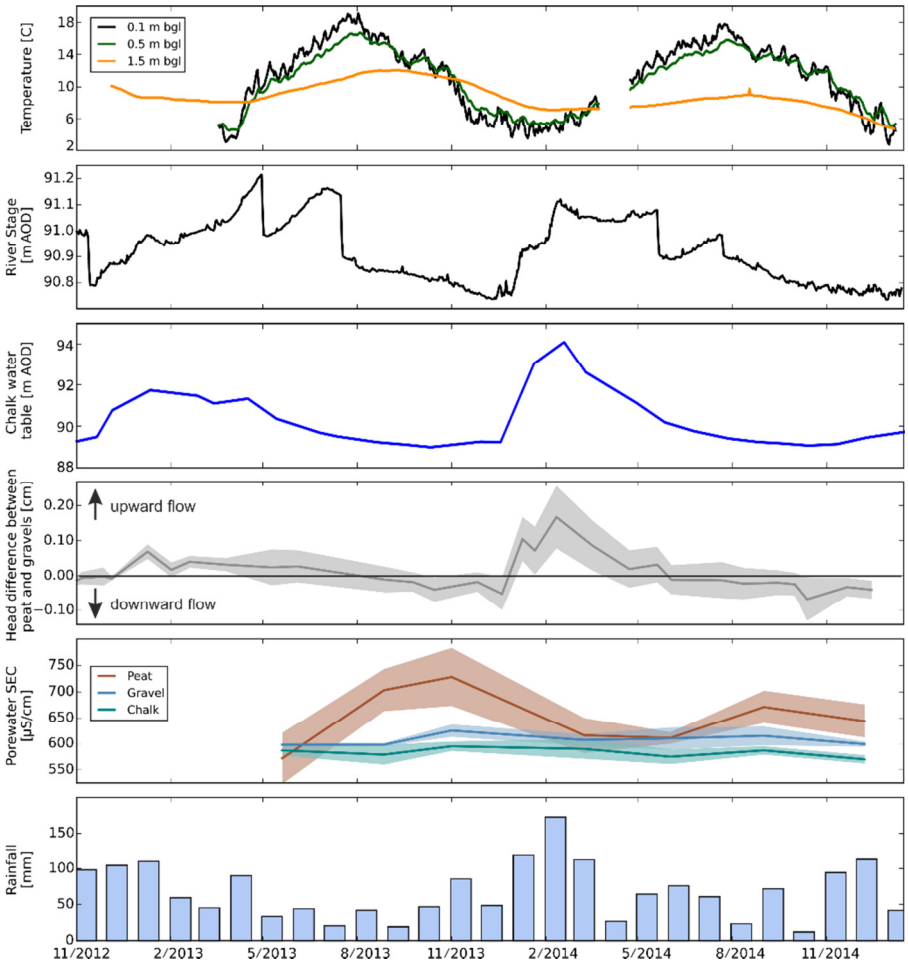

363

364 **Figure 5** Multi-level temperature data from the weather station, river stage, head in the chalk, vertical head differential
365 between the gravel and peat, pore water SEC for peat, gravel, and chalk, and monthly rainfall data for the monitoring
366 period. Vertical head differentials and pore water SEC show mean values across all locations (see Figure 1); shaded areas
367 indicate range. Note that peat pore water SEC values are derived from aggregated water samples and thus represent
368 averaged values.

369 ## 3.2. ERI Monitoring

370 The resistivity models of the baseline measurements t_0 (December 2012) show low resistivity
371 alluvium (cold colors, ρ < 30Ωm), mainly consisting of peat, overlying more resistive clean gravels
372 (warm colors, ρ > 55 Ωm) for both the northern and southern meadow (Figure **6**). The boundary
373 between these two materials is imaged very sharply at the northern meadow and coincides with
374 intrusively determined peat thicknesses [*Chambers et al.*, 2014b]. For the southern meadow,

however, this boundary is less pronounced, which is likely to be an effect of reduced sensitivity of the ERI method at depth caused by the use of a shorter electrode array.

Within the peat layer of the northern meadow, two areas of anomalously low resistivity are evident at profile distances *x* of 6 - 12 m and 20 – 26 m. These can be interpreted as structures having a higher degree of more recent fine material and organic infill, and coincide with channel structures imaged by Chambers et al. [2014b] . The low resistivity anomaly at $x > 12$ m of the southern meadow is a similar channel feature. Within the gravels of the northern meadow between 10 m and 16 m a resistive anomaly can be found, which is likely to be caused by gravels of lower porosity.

To highlight changes in the resistivity models, the proceeding time steps of Figure **6** are shown as resistivity changes between two consecutive time steps (i.e. change between t_2 and t_1, t_4 and t_3, etc.), with blue/red colors indicating decreasing/increasing resistivities respectively. Throughout the monitoring period, resistivity changes showed significant amplitudes of -50 % to +100 %, equal to a reduction to half or an increase to twice the initial value, respectively (note that the color scale of Figure **6** has been limited to values ranging from -30 % – +40 %). Thus, these values are well above likely noise levels of the ERI changes, which were calculated to be ±9.8 %.

Within the peat, there are two layers that appear to behave differently according to the hydrological conditions. This is particularly clear at time step t_1 from December 2012 to April 2013 (Figure 6) when the peat heads rose towards their annual maximum. In the upper layer (0.0 m – 0.5 m bgl) resistivities were decreasing, whilst in the lower layer (> 0.5 m bgl) resistivities were increasing. This trend continued through time steps t_2 and t_3 (May to June 2013). By time step t_4, peat heads had dropped by 0.25 m in November 2013 as a result of weed cutting in July 2013, which coincided with an increasing resistivity of the upper layer and decreasing resistivity of the lower layer. There was generally decreasing resistivity within the lower layer through time step t_5. These ERI observations correlate with the bulk resistivity sensor data over this period (*Pearson r* = 0.65; Figure 4).

High water table conditions were re-established in the peat by January 2014 and there is evidence for the layered cycle in resistivity observed between t_0 and t_5 recommencing. At t_6 (March to April 2014), resistivities were decreasing and increasing in the upper layer and lower layer, respectively, when the upward vertical head differentials reach their maximum across the site (Figure 5). Although weed cutting occurred in May 2014 and led to a drop in peat heads of about 0.15 m, resistivity changes at t_7 (April to July 2014) showed a continuation and amplification of the trends of t_6. Following the drop in heads near to the annual minimum at time step t_8, caused by a weed cut in July 2014, resistivity trends within the layers reversed: increasing in the upper layer and declining in the lower layer, as observed at time step t_4.

The gravels, mainly imaged at the northern meadow, showed more spatially-consistent temporal changes. At t_1 a reduction in resistivity compared to the baseline measurement can be observed, which is highest just below the channel features imaged in the peat (t_0). This trend continued through to time step t_3, where only minor resistivity changes were found in the gravels. Strongly decreasing resistivities can be found at t_5 (September 2013 to March 2014), coinciding with a rise in peat heads and river stage (Figures 4 and 5, respectively). This was followed by only minor changes at t_6 and minor resistivity decreases throughout t_7 and t_8. Nearly throughout the entire monitoring period an area between x = 16 m – 21 m formed a discontinuity of the resistivity trends in the gravels of the northern meadow.

Analyses of pore waters from the peat and gravels provided representative conductivities of σ_{pw} = 900 µS/cm and σ_{gw} = 600 µS/cm for the peat and gravel, respectively. The mean resistivities of the lower peat layer showed a change from 24.8 Ωm to 32.6 Ωm during the upwelling period from February to July. Assuming that the pore waters and surface conductance σ_{surf} can be represented as resistors in a parallel circuit, the peat conductivity can be defined as [modified from *Comas and Slater*, 2004]:

(4)

$$\sigma_{peat} = \left(\frac{1}{F}\right)\left(a\sigma_{pw} + b\sigma_{gw}\right) + \sigma_{surf}$$

423 with *a* and *b* defining the fraction of the pore space occupied by pore water representative for peat
424 or gravel, respectively, and *F* being the formation factor. Note, σ_{surf} was derived from data published
425 by Comas and Slater [2004]. Employing the representative pore water conductivities of peat and
426 gravels, it can be calculated that the pore water in the lower peat consists of 94% gravel and 6% peat
427 pore water at the peak of upwelling. This assumes (1) no ingress of surface waters into the lower
428 peat, which is reasonable given the lack of inundation, as well as both the low permeability of the
429 peat and lateral distance between the arrays and nearest surface waters, and (2) that the pore water
430 in February consisted of peat pore water only.

431 Changes corresponding to the first part (i.e. reduction and increase of the resistivities of the upper
432 and lower layers, respectively) and second part of the cycle (i.e. increasing and decreasing resistivity
433 of the upper and lower layers, respectively) seem more pronounced in the first monitoring year
434 (Figure 6). This could probably be related to uncommonly dry conditions preceding the start of the
435 ERI monitoring and thus larger changes caused by groundwater recharge to the system.

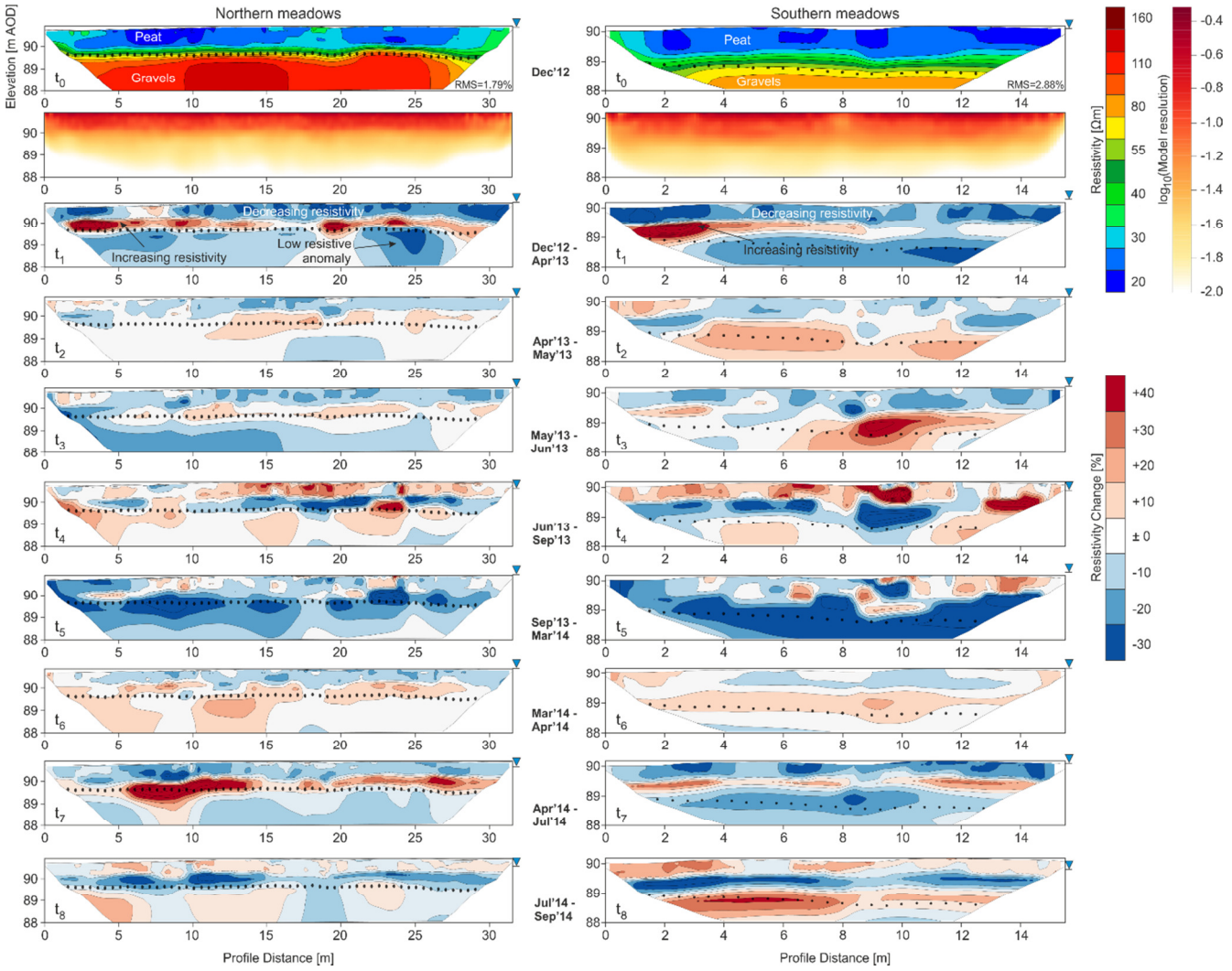

436

437 **Figure** 6 Baseline resistivity measurements (t_0), model resolution, and measurements of eight proceeding time steps of the
438 northern and southern meadow. Dates of the measurements are indicated in Figure 4. The time steps proceeding the
439 baseline results are shown as resistivity changes between two consecutive time steps (i.e. between t_2 and t_1, t_4 and t_3, etc.).
440 Blue colors indicate decreasing resistivity, while red colors indicate increasing resistivity. Dotted line shows intrusively
441 determined interface between peat and the underlining gravel (from Chambers et al. [2014b]). The water table is indicated
442 on the right at each time step.

443 ### 3.3. Shrink-swell characterization

444 Episodes of shrink-swell indicated by surface elevation correlate with drying-wetting cycles
445 (Pearson's r = 0.52; Figure 7). RTK-GPS measurements demonstrate a change in average topographic
446 elevation (and thus peat thickness) of up to 0.10 m in the northern meadow. Inspection of the
447 boundary extraction of peat thicknesses highlights a similar relationship, with periods of high and

low peat thicknesses corresponding to water table highs and lows, respectively. Good correlation is indicated by a Pearson's *r* correlation coefficient of 0.80. Results of the two approaches to extract the peat thickness (temporally variable and constant clusters) are comparable. These show the average peat thickness cycling between 0.98 and 1.12 m, in line with the topographic range.

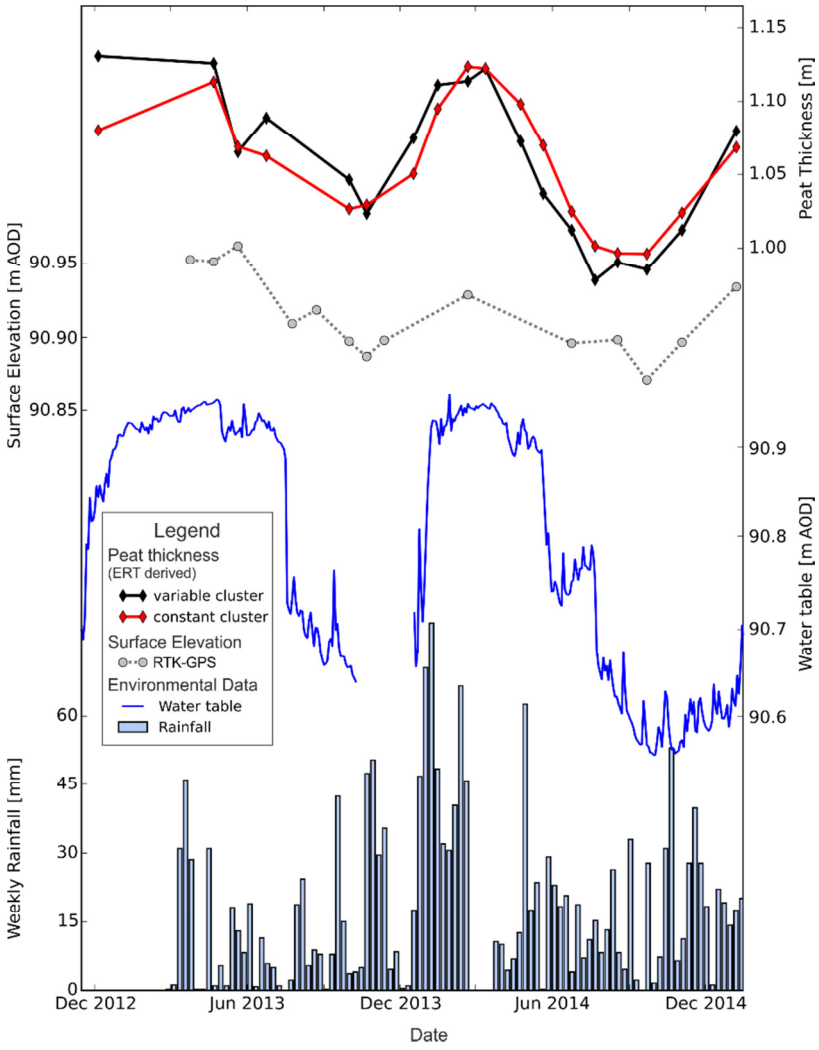

Figure 7 Comparison of average peat thickness estimates. Peat thickness was derived from boundary extraction from the ERI models. Surface elevation (determined using RTK-GPS) is representative for changes in peat thickness, assuming that the peat-gravel interface is constant in space. Note the good correlation between peat thickness and water table.

4. Discussion

4.1. Imaging plant transpiration or microbial activity?

458 The decreasing resistivity of the upper peat layer from winter to spring is most likely to be caused by
459 changes in pore water conductivity. This is because (1) the moisture content remained at a constant
460 high during the two imaged seasons, thus indicating fully saturated conditions, and (2) temperature
461 variations, which would have resulted in the inverse trend anyhow, were corrected for. Pore water
462 conductivity dynamics may have been induced by vegetation or microbial activity.

463 Plant transpiration may result in the accumulation of superfluous minerals, which would not readily
464 be flushed given the relatively low permeability. Vegetation around the arrays is dominated by
465 deciduous reed sweet-grass (*Glyceria maxima*) and lesser pond-sedge (*Carex acutiformis*). These
466 species die back during winter; hence, photosynthesis (and transpiration) will only initiate following
467 the onset of new leaf growth in spring. Both species root sufficiently deeply to uptake water from
468 the majority of the peat profile [*Atwell et al.*, 1980; *USDA*, 2007], which is inconsistent with the
469 decreases in resistivity in only the upper part of the peat (Figure 8). Nevertheless, the majority of
470 water uptake is likely to be from the near-surface given the greater density of roots near the stem
471 and the perennial availability of water within 0.1 m of the surface negating the need for deep roots
472 at this site.

473 Microbial activity in the near-surface could contribute to a decrease of the pore water resistivity
474 through the dissolution of minerals from the organic matrix [*Atekwana and Slater*, 2009; *House et*
475 *al.*, 2015]. Higher numbers of microbes are frequently observed near the surface or in close
476 proximity to the water table [*Sundh et al.*, 1994; *Daulat and Clymo*, 1998; *Fisk et al.*, 2003]. This is
477 likely to be the case here, where vegetation dieback around November produces a mass of black
478 litter that represents a readily available carbon food source at the surface. Furthermore, the greater
479 density of roots in this horizon would also enhance oxygen availability, as well as food supply
480 through release of exudates containing significant quantities of carbon [*Bertin et al.*, 2003; *Mainiero*
481 *and Kazda*, 2005].

Seasonality in microbial activity is likely to be primarily driven by rising subsurface temperatures in the spring [*Picard et al.*, 2005]. In winter, temperatures stabilize around 5^{o}C, often termed "biological zero" where biological processes in wetlands dramatically slow down or cease [*Mitsch and Gosselink*, 2007]. Furthermore, exudates and oxygen release from roots in the subsurface are greatest during photosynthesis [*Watson et al.*, 1997; *Kuzyakov and Cheng*, 2001]. The near-surface horizon remains perennially saturated with moisture contents high, so any water table dynamics are unlikely to be a key driver of microbial activity, unlike other well-drained peatland ecosystems [e.g. *Moore et al.,* 2007*]*.

Root respiration in the soil is also likely to be a contributing factor to near-surface resistivity dynamics, which has been demonstrated to account for around 35-50% of temperate ecosystem respiration in peatlands [*Silvola et al.*, 1996; *Lafleur et al.*, 2005]. The release and subsequent dissolution of CO_2, could lower pore water pH and increase mineral weathering. This would be most likely to be restricted to the near-surface horizon due to greater root density and relate seasonally to the start of photosynthesis and correlate with air temperatures, thereby peaking in summer [*Phillips et al.*, 2010]. However, subsurface production of CO_2 and other gases such as methane has been shown to increase resistivity by replacing the conductive water within the pore spaces with non-conductive gases [*Slater et al.*, 2007]. This process is most likely to cause the increase in resistivity during the summer season after the fall in water table, when free-phase gases produced in deeper peat layers are released [*Bon et al.*, 2014]. However, this fall in water table also results in significant reduction of moisture content in the upper 0.1 m, which will affect the resistivity signature to a higher degree.

While all of these processes are likely to cause the imaged changes in pore water conductivity, no biogeochemical data were available to define their specific contributions. This will be investigated in further work, employing peat sampling and biogeochemical analysis, monitoring of gas production, and automated, 3-D ERI monitoring of the root zone.

4.2. Imaging groundwater exchange or biogenic gas production?

The strong increases in resistivity between winter and spring in the lower peat layer are most likely to be a result of the upwelling of more resistive, deeper groundwater. As this period is concomitant with maximum moisture content and the resistivity data are corrected for seasonal temperature contrasts, changes in type of pore fluid are the most likely explanation. This is evidenced by data from cluster 2 in the northern meadow (Figure 8), where a sudden rise in temperature (indicative for upwelling of deeper groundwater) coincides with increasing bulk resistivities. Hydrological observations also demonstrate a transition to positive vertical head differentials, a bulk reduction in peat electrical conductivity, and peat pore water SEC becoming more akin to the gravels and chalk over this period (Figure 5). The fact that these resistivity dynamics are restricted to only the lower peat layer again indicates that the thin chalky clay is significant in minimizing water exchange. However, following riverine weed cutting and the lowering of surface water stage encircling the site, the shallow conductive waters that have developed in the shallow peat layer appear to drain into the deeper peats. This is suggested by an increase in resistivity of the upper and decrease in resistivity of the lower layer (Figure 9). Therefore, groundwater exchange between the layers may be possible when there is a large hydraulic head differential, such as post weed cutting (Figure 10).

Another possible explanation for the the deeper peat resistivity variations is biongenic gas production and consequent dynamics of free-phase gases (FPG). While an accumulation of FPG will be indicated by an increase in resistivity, FPG release will show a decreasing signature [*Slater et al.*, 2007]. Accumulation is likely to take place during the spring and summer, with release most likely taking place after the drop in water level in response to the riverine weed cutting. This generally follows the pattern imaged in the lower layer (Figure 9). Accumulation and subsequent release of FPGs could also be a driver for the imaged changes in peat thickness (Figure 7). However, no short-term oscillations in hydraulic head that is indicative for FPG ebullition were observed at site. The peatland studied by Parsekian et al. [2011] showed the majority of gas production to occur below

2.5 m depth and be dependent on the vegetation type. Fen-dominated peatlands, as the Lambourn observatory, showed a homogeneous FPG distribution with FPG occupying between 0 – 7 % of the pore space. Thus, the effect of FPGs on the imaged resistivity variations is likely to be limited. However, no direct measurements of released gases were obtained, but will be part of a forthcoming study.

Also expansion and compaction of the peat are likely to influence its resistivity signature, due to increasing and decreasing pore space, respectively. While peat thicknesses are shown to correlate well with changes in water table, the resistivity signature of the lower peat is, in comparison, out of phase. Thus peat shrink-swell is unlikely to have a major influence on the imaged resistivity variations.

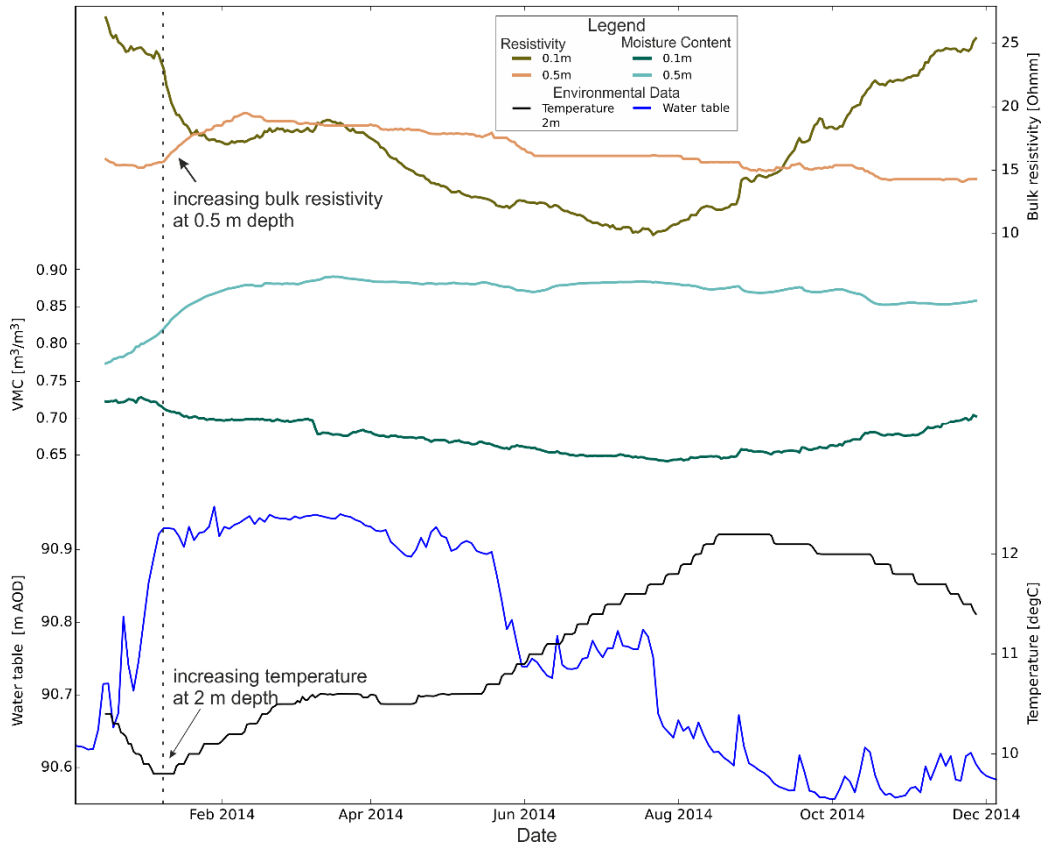

Figure 8 Data of sensor cluster 2 of the northern meadow. Note the sudden change in temperature in February 2014, which correlates with increasing resistivities in the deeper peat. Bulk resistivities of upper (0.1 m) and lower (0.5 m) peat show differing temporal trends which are in agreement with ERI monitoring data.

The decreasing resistivities imaged in the gravels just below the most pronounced indications of upwelling in the lower peat layer in spring 2014, may have been caused by the elevated temperature of upwelling groundwater. Although the presented data are corrected for seasonal temperature variations, localized temperature anomalies of up to 5°C (temperature contrast between peat and gravel during winter; Figures 5 and 8) would induce resistivity variations of up to 10%. The very low gravel resistivity in March 2014 coincides with the smallest vertical head differentials, and may therefore indicate a continued transfer of conductive surface waters through the lower peat layer into the gravels. The discontinuity imaged within the gravels (16 m < x < 21 m) is likely to be an area of reduced porosity, where, due to the smaller available pore space, changes in pore water conductivity are less pronounced than in the surrounding higher porosity gravels. However, as the sensitivity of ERI reduces with increasing distance from the electrodes (and thus depth), uncertainties of the processes imaged in the gravels are higher than in the peat layers.

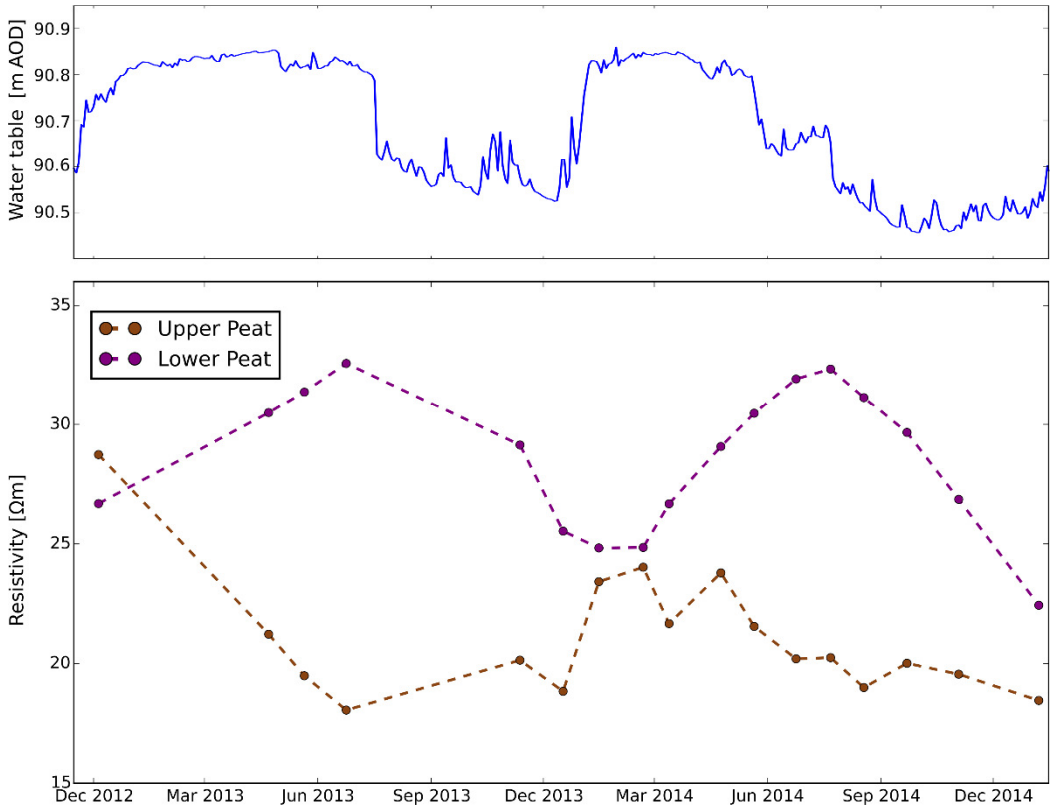

Figure 9 Water table and time series of mean resistivities of the upper and lower peat layer, highlighting the seasonal changes.

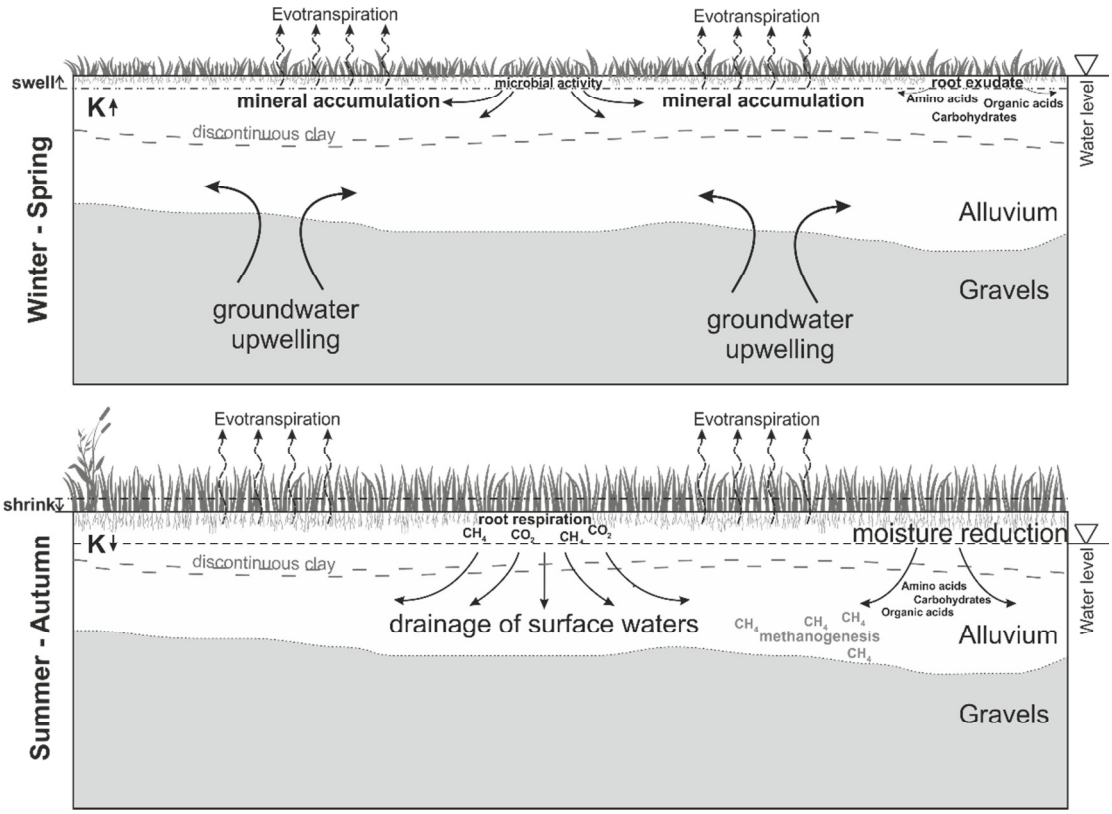

561

562 **Figure 10** Conceptual diagram showing the processes characterizing periods of groundwater upwelling and drainage of
563 surface waters, as well as peat shrink-swell and its effect on the hydraulic conductivity K.

564 ### 4.3. Imaging shrink-swell

565 As shown by Price and Schlotzhauer [1999], shrink-swell behavior of the peat shows a clear
566 correlation with the peat water table which is therefore the main driver for this process. RTK-GPS
567 measurements showed a cyclic behavior with average topographic heights varying by about 0.10 m,
568 being greater than the instrument precision that was determined to be 0.03 m. This indicates a
569 variation of 7-10 % of the total peat thickness, values that are comparable to studies of peatlands in
570 the Netherlands [*Hoogland et al.*, 2012; *Querner et al.*, 2012] and Canada [*Price and Schlotzhauer*,
571 1999]. Very similar ranges were found for ERI derived peat thicknesses. The smooth variation of
572 these in time is likely to be caused by the data inversion methodology, which favors smooth
573 temporal changes. Note that the model cell size at the depth of the peat interface is larger than the
574 imaged variations of peat thickness (0.25 m and 0.14 m, respectively). Therefore, estimation of the
575 small thickness variation was only possible due to the sharp geological interface between peat and

576 gravels that also showed a very strong contrast in resistivity (20 Ωm to 150 Ωm). Thus, resistivity
577 values of the model cells close to the interface will show significant variations with changing layer
578 thickness, and therefore a trackable boundary.

579 For only 1 % change in peat thickness Price [2003] found a change in hydraulic conductivity of two
580 orders of magnitude. Hence, the 7 – 10 % change observed at the Lambourn observatory are likely
581 to cause even larger changes, with decreasing hydraulic conductivity in summer due to compaction
582 and increasing conductivity in winter caused by peat expansion. This will not only restrict moisture
583 uptake by plants in summer due to a decreased vertical moisture fluxes and thus affect the
584 vegetation community, but also highlights the need to incorporate seasonally varying hydraulic
585 parameters in hydrologic models of peatlands.

586 The recent development of automated remote monitoring systems and analysis tools offers the
587 potential to monitor peat thickness variations at high temporal resolution without the need of
588 additional surface elevation monitoring instrumentation. Thus, less instrumentation needs to be
589 installed and study sites can be operated more economically.

590 5. Conclusions

591 The application of time-lapse geoelectrical imaging in an ecologically sensitive riparian wetland has
592 revealed a two-layer hydrological system within the peat, which is considered a result of a thin
593 intermediate chalky clay layer. Layered groundwater systems are likely to be widespread in riparian
594 wetlands [*Hunt et al.*, 1996; *Letts et al.*, 2000] given the varied depositional history in floodplain
595 environments. Resistivity dynamics within the two layers follow separate annual cycles relating to
596 the dominating influence from different processes.

597 The upper layer is characterized by a resistivity reduction in spring (March to June) when saturated,
598 resulting from processes affecting the pore water conductivity, including microbial activity, plant
599 transpiration, and root respiration. Following aquatic weed cutting around June/July, and a drop in

600 the encircling surface water stage, resistivities increase as water drains from the upper peat and the
601 moisture content decreases. In the lower layer, resistivities increase around February due to the
602 influx of more resistive groundwater from the underlying gravels during the seasonal groundwater
603 high. Following the cessation of deeper groundwater input, the conductive water in the upper peat
604 then drains into this lower layer following the weed cutting [*Old et al.*, 2014], thereby reducing the
605 resistivity.

606 The additional sensor data facilitated a detailed understanding of the geophysical data. A sole,
607 independent interpretation of either data would not have provided the same level of detail to
608 investigate the hydrological processes. Notably, the main benefit of the geoelectrical data is its non-
609 invasive, spatial nature, which was able to visualize the dynamic vertical and lateral extent of
610 multiple hydrological processes and guide the installation of additional sensors to investigate them.

611 For the first time, we have shown that applying automated interface detection algorithms to time-
612 lapse ERI models can reveal the migration of a geological interface in the vertical direction. This is
613 demonstrated through the observation of shrink-swell within the peat, which is calculated to be
614 similar to that observed through topographic changes at the surface. The conjunction of time-lapse
615 geoelectrical imaging with automated interface detection algorithms could be useful for studying
616 ground movement more broadly, including phenomena such as subsidence, ground heave, or
617 landslides. Whilst ground movement can easily be observed using current surface based techniques
618 such as laser scanning and time-lapse cameras, ERI could provide data with comparable accuracy
619 and information on where in the subsurface movements are induced.

620 A subsequent study will quantify the contributions of the presented possible factors affecting the
621 resistivity dynamics of the upper and lower peat layer, including 4-D ERI monitoring with high
622 temporal resolution, extraction of peat samples for biogeochemical analysis, and measurements of
623 gas fluxes.

6. Acknowledgements

We would like to thank the Editor (Jean Bahr), the Associate Editor, Neil Terry and two anonymous reviewers for their helpful comments on our original manuscript. This paper is published with the permission of the Executive Director of the British Geological Survey (NERC). The analyzed data are archived by the British Geological Survey, and are available from the authors.

7. References

Allen, D. J., W. G. Darling, D. C. Gooddy, D. J. Lapworth, A. J. Newell, A. T. Williams, D. Allen, and C. Abesser (2010), Interaction between groundwater, the hyporheic zone and a Chalk stream: A case study from the River Lambourn, UK, *Hydrogeol. J.*, *18*(5), 1125–1141, doi:10.1007/s10040-010-0592-2.

Archie, G. E. (1942), The electrical resistivity log as an aid in determining some reservoir characteristics, *Pet. Trans. AIME*, *146*, 54–62.

Atekwana, E. A., and L. D. Slater (2009), Biogeophysics: A new frontier in Earth science research, *Rev. Geophys.*, *47*(4), 1–30, doi:10.1029/2009RG000285.

Atwell, B. J., M. T. Veerkamp, B. Stuiver, and P. J. C. Kuiper (1980), The Uptake of Phosphate by Carex Species From Oligotrophic to Eutrophic Swamp Habitats, *Physiol. Plant.*, *49*(4), 487–494.

Audebert, M., R. Clément, N. Touze-foltz, T. Günther, S. Moreau, and C. Duquennoi (2014), Time-lapse ERT interpretation methodology for leachate injection monitoring based on multiple inversions and a clustering strategy (MICS), *J. Appl. Geophys.*, *111*, 320–333, doi:10.1016/j.jappgeo.2014.09.024.

Ausden, M., W. J. Sutherland, and R. James (2001), The effects of flooding lowland wet grassland on soil macroinvertebrate prey of breeding wading birds, *J. Appl. Ecol.*, *38*(2), 320–338, doi:10.1046/j.1365-2664.2001.00600.x.

Baldwin, A. H., M. S. Egnotovich, and E. Clarke (2001), Hydrologic change and vegetation of tidal freshwater marshes: Field, greenhouse, and seed-bank experiments, *Wetlands*, *21*(4), 519–531, doi:10.1672/0277-5212(2001)021[0519:HCAVOT]2.0.CO;2.

Bertin, C., X. Yang, and L. a Weston (2003), The role of root exudates and ellelochemicals in the rhizosphere, *Plant Soil*, *256*, 67–83.

Binley, A., S. S. Hubbard, J. a Huisman, A. Revil, D. a Robinson, K. Singha, and L. D. Slater (2015), The emergence of hydrogeophysics for improved understanding of subsurface processes over multiple scales, *Water Resour. Res.*, *51*, doi:10.1002/2015WR017016.

Bloom, A. A., P. I. Palmer, A. Fraser, D. S. Reay, and C. Frankenberg (2010), Large-Scale Controls of Methanogenesis Inferred from Methane and Gravity Spaceborne Data, *Science (80-.).*, *327*(5963), 322–325, doi:10.1126/science.1175176.

Bon, C. E., a. S. Reeve, L. Slater, and X. Comas (2014), Using hydrologic measurements to investigate free-phase gas

ebullition in a Maine peatland, USA, *Hydrol. Earth Syst. Sci.*, *18*(3), 953–965, doi:10.5194/hess-18-953-2014.

Bradley, C. (1997), The hydrological basis for conservation of floodplain wetlands: Implications of work at Narborough Bog, UK, *Aquat. Conserv. Mar. Freshw. Ecosyst.*, *7*(June 1996), 41–62.

Bridgham, S. D., H. Cadillo-Quiroz, J. K. Keller, and Q. Zhuang (2013), Methane emissions from wetlands: Biogeochemical, microbial, and modeling perspectives from local to global scales, *Glob. Chang. Biol.*, *19*(5), 1325–1346, doi:10.1111/gcb.12131.

Cardenas, M. B., and M. S. Markowski (2011), Geoelectrical imaging of hyporheic exchange and mixing of river water and groundwater in a large regulated river, *Environ. Sci. Technol.*, *45*(4), 1407–1411, doi:10.1021/es103438a.

Chambers, J., D. Gunn, P. B. Wilkinson, P. I. Meldrum, E. Haslam, S. Holyoake, M. Kirkham, O. Kuras, A. Merritt, and J. Wragg (2014a), 4D electrical resistivity tomography monitoring of soil moisture dynamics in an operational railway embankment, *Near Surf. Geophys.*, *12*(2007), doi:10.3997/1873-0604.2013002.

Chambers, J. E., R. Ogilvy, and O. Kuras (2002), 3D electrical imaging of known targets at a controlled environmental test site, *Environ. Geol.*, *41*(6), 690–704, doi:10.1007/s00254-001-0452-4.

Chambers, J. E. et al. (2012), Bedrock detection beneath river terrace deposits using three-dimensional electrical resistivity tomography, *Geomorphology*, *177-178*, 17–25.

Chambers, J. E. et al. (2014b), Derivation of lowland riparian wetland deposit architecture using geophysical image analysis and interface detection, *Water Resour. Res.*, *50*(7), 5886–5905, doi:10.1002/2014WR015643.

Chambers, J. E. et al. (2015), Spatial monitoring of groundwater drawdown and rebound associated with quarry dewatering using automated time-lapse electrical resistivity tomography and distribution guided clustering, *Eng. Geol.*, *193*, 412–420, doi:10.1016/j.enggeo.2015.05.015.

Chow, T. L., H. W. Rees, I. Ghanem, and R. Cormier (1992), Compactibility of Cultivated Sphagnum Peat Material and Its Influence on Hydrologic Characteristics, *Soil Sci.*, *153*(4), 300–306.

Chrétien, M., J. F. Lataste, R. Fabre, and a. Denis (2014), Electrical resistivity tomography to understand clay behavior during seasonal water content variations, *Eng. Geol.*, *169*, 112–123, doi:10.1016/j.enggeo.2013.11.019.

Comas, X., and L. Slater (2004), Low-frequency electrical properties of peat, *Water Resour. Res.*, *40*(12), 1–9, doi:10.1029/2004WR003534.

Comas, X., L. Slater, and A. Reeve (2004), Geophysical evidence for peat basin morphology and stratigraphic controls on vegetation observed in a Northern Peatland, *J. Hydrol.*, *295*(1-4), 173–184, doi:10.1016/j.jhydrol.2004.03.008.

Comas, X., L. Slater, and a. S. Reeve (2011), Pool patterning in a northern peatland: Geophysical evidence for the role of postglacial landforms, *J. Hydrol.*, *399*(3-4), 173–184, doi:10.1016/j.jhydrol.2010.12.031.

Dahlin, T., and B. Zhou (2004), A numerical comparison of 2D resistivity imaging with 10 electrode arrays, *Geophys. Prospect.*, *52*(5), 379–398, doi:10.1111/j.1365-2478.2004.00423.x.

Daulat, W. E., and R. S. Clymo (1998), Effects of temperature and watertable on the efflux of methane from peatland surface cores, *Atmos. Environ.*, *32*(19), 3207–3218, doi:10.1016/S1352-2310(98)00078-8.

Davidson, N. C. (2014), How much wetland has the world lost? Long-term and recent trends in global wetland area, *Mar.*

690 *Freshw. Res.*, *65*(10), 934–941, doi:http://dx.doi.org/10.1071/MF14173.

691 EEC (1992), *Habitats Directive 92/43/EEC*, EEC, Brussels.

692 Fisk, M. C., K. F. Ruether, and J. B. Yavitt (2003), Microbial activity and functional composition among northern peatland
693 ecosystems, *Soil Biol. Biochem.*, *35*(4), 591–602, doi:10.1016/S0038-0717(03)00053-1.

694 Gilliam, J. W. (1994), Riparian Wetlands and Water Quality, *J. Environ. Qual.*, *23*(5), 896,
695 doi:10.2134/jeq1994.00472425002300050007x.

696 Gorham, E. (1995), The biochemistry of northern peatlands and its possible responses to global warming, in *Biotic*
697 *Feedbacks in the Global Climate System*, edited by G. M. Woodwell and F. T. Mackenzie, pp. 169–187, Oxford
698 University Press, Oxford.

699 Gunn, D. A. et al. (2014), Moisture monitoring in clay embankments using electrical resistivity tomography, *Constr. Build.*
700 *Mater.*, *92*, 82–94, doi:10.1016/j.conbuildmat.2014.06.007.

701 Hayashi, M. (2004), Temperature-electrical conductivity relation of water for environmental monitoring and geophysical
702 data inversion, *Environ. Monit. Assess.*, *96*, 119–128.

703 Hayley, K., L. R. Bentley, M. Gharibi, and M. Nightingale (2007), Low temperature dependence of electrical resistivity:
704 Implications for near surface geophysical monitoring, *Geophys. Res. Lett.*, *34*(18), L18402,
705 doi:10.1029/2007GL031124.

706 Hermans, T., S. Wildemeersch, P. Jamin, P. Orban, S. Brouyère, A. Dassargues, and F. Nguyen (2015), Quantitative
707 temperature monitoring of a heat tracing experiment using cross-borehole ERT, *Geothermics*, *53*, 14–26,
708 doi:10.1016/j.geothermics.2014.03.013.

709 Holden, J., and T. P. Burt (2002), Piping and pipeflow in a deep peat catchment, *Catena*, *48*(3), 163–199,
710 doi:10.1016/S0341-8162(01)00189-8.

711 Hoogland, T., J. J. H. van den Akker, and D. J. Brus (2012), Modeling the subsidence of peat soils in the Dutch coastal area,
712 *Geoderma*, *171-172*, 92–97, doi:10.1016/j.geoderma.2011.02.013.

713 House, A. R., J. P. R. Sorensen, D. C. Gooddy, A. J. Newell, B. Marchant, J. O. Mountford, P. Scarlett, P. J. Williams, and G. H.
714 Old (2015), Discrete wetland groundwater discharges revealed with a three-dimensional temperature model and
715 botanical indicators (Boxford, UK), *Hydrogeol. J.*, doi:10.1007/s10040-015-1242-5.

716 Hunt, R. J., D. P. Krabbenhoft, and M. P. Anderson (1996), Groundwater inflow measurements in wetland systems, *Water*
717 *Resour. Res.*, *32*(3), 495–507, doi:10.1029/95WR03724.

718 Kehew, A. E., R. N. Passero, R. V Krishnamurthy, C. K. Lovett, M. A. Betts, and B. A. Dayharsh (1998), Hydrogeochemical
719 interaction between a wetland and an unconfined glacial drift aquifer, Southwestern Michigan, *Ground Water*, *36*(5),
720 849–856.

721 Kennedy, G. W., and J. S. Price (2005), A conceptual model of volume-change controls on the hydrology of cutover peats, *J.*
722 *Hydrol.*, *302*(1-4), 13–27, doi:10.1016/j.jhydrol.2004.06.024.

723 Kettridge, N., X. Comas, A. Baird, L. Slater, M. Strack, D. Thompson, H. Jol, and A. Binley (2008), Ecohydrologically important
724 subsurface structures in peatlands revealed by ground-penetrating radar and complex conductivity surveys, *J.*
725 *Geophys. Res. Biogeosciences*, *113*(4), 1–15, doi:10.1029/2008JG000787.

Killeen, I. J. (2003), *Ecology of Desmoulin's Whorl Snail: Vertigo Moulinsiana*, Conserving Natura 2000 Rivers Ecology Series, English Nature.

Kim, J.-H., M.-J. Yi, S.-G. Park, and J. G. Kim (2009), 4-D inversion of DC resistivity monitoring data acquired over a dynamically changing earth model, *J. Appl. Geophys.*, *68*(4), 522–532, doi:10.1016/j.jappgeo.2009.03.002.

Koestel, J., A. Kemna, M. Javaux, A. Binley, and H. Vereecken (2008), Quantitative imaging of solute transport in an unsaturated and undisturbed soil monolith with 3-D ERT and TDR, *Water Resour. Res.*, *44*(12), n/a–n/a, doi:10.1029/2007WR006755.

Kuras, O., J. D. Pritchard, P. I. Meldrum, J. E. Chambers, P. B. Wilkinson, R. D. Ogilvy, and G. P. Wealthall (2009), Monitoring hydraulic processes with automated time-lapse electrical resistivity tomography (ALERT), *Comptes Rendus Geosci.*, *341*(10-11), 868–885, doi:10.1016/j.crte.2009.07.010.

Kuzyakov, Y., and W. Cheng (2001), Photosynthesis controls of rhizosphere respiration and organic matter decomposition, *Soil Biol. Biochem.*, *33*(14), 1915–1925, doi:10.1016/S0038-0717(01)00117-1.

LaBrecque, D. J., M. Miletto, W. Daily, A. Ramirez, and E. Owen (1996), The effects of noise on Occam's inversion of resistivity tomography data, *Geophysics*, *61*(2), 538–548.

Lafleur, P. M., T. R. Moore, N. T. Roulet, and S. Frolking (2005), Ecosystem respiration in a cool temperate bog depends on peat temperature but not water table, *Ecosystems*, *8*(6), 619–629, doi:10.1007/s10021-003-0131-2.

Letts, M. G., N. T. Roulet, N. T. Comer, M. R. Skarupa, and D. L. Verseghy (2000), Parametrization of peatland hydraulic properties for the Canadian land surface scheme, *Atmosphere-Ocean*, *38*(1), 141–160, doi:10.1080/07055900.2000.9649643.

Limpens, J., F. Berendse, C. Blodau, J. G. Canadell, C. Freeman, J. Holden, N. Roulet, H. Rydin, and G. Schaepman-Strub (2008), Peatlands and the carbon cycle: from local processes to global implications – a synthesis, *Biogeosciences*, *5*(2), 1379–1419, doi:10.5194/bgd-5-1379-2008.

Loke, M., and R. Barker (1996), Practical techniques for 3D resistivity surveys and data inversion, *Geophys. Prospect.*, *44*, 499–523.

Lowry, C. S., D. Fratta, and M. P. Anderson (2009), Ground penetrating radar and spring formation in a groundwater dominated peat wetland, *J. Hydrol.*, *373*(1-2), 68–79, doi:10.1016/j.jhydrol.2009.04.023.

Ma, R., A. McBratney, B. Whelan, B. Minasny, and M. Short (2010), Comparing temperature correction models for soil electrical conductivity measurement, *Precis. Agric.*, *12*(1), 55–66, doi:10.1007/s11119-009-9156-7.

Mainiero, R., and M. Kazda (2005), Effects of Carex rostrata on soil oxygen in relation to soil moisture, *Plant Soil*, *270*(1), 311–320, doi:10.1007/s11104-004-1724-z.

Marsh, T. J., and J. Hannaford (2008), *UK Hydrometric Register. Hydrological data UK series*, Centre for Ecology & Hydrology.

Martinez-Martinez, E., a. P. Nejadhashemi, S. a. Woznicki, and B. J. Love (2014), Modeling the hydrological significance of wetland restoration scenarios, *J. Environ. Manage.*, *133*, 121–134, doi:10.1016/j.jenvman.2013.11.046.

McMenamin, S. K., E. a Hadly, and C. K. Wright (2008), Climatic change and wetland desiccation cause amphibian decline in Yellowstone National Park., *Proc. Natl. Acad. Sci. U. S. A.*, *105*(44), 16988–16993, doi:10.1073/pnas.0809090105.

762 Mitsch, W. J. (1992), Landscape design and the role of created, restored, and natural riparian wetlands in controlling
763 nonpoint source pollution, *Ecol. Eng.*, *1*(1-2), 27–47, doi:10.1016/0925-8574(92)90024-V.

764 Mitsch, W. J., and J. G. Gosselink (2007), *Wetlands*, 4th Editio., Wiley, New York.

765 Mitsch, W. J., B. Bernal, A. M. Nahlik, Ü. Mander, L. Zhang, C. J. Anderson, S. E. Jørgensen, and H. Brix (2013), Wetlands,
766 carbon, and climate change, *Landsc. Ecol.*, *28*(4), 583–597, doi:10.1007/s10980-012-9758-8.

767 Moore, T. R., J. L. Bubier, and L. Bledzki (2007), Litter decomposition in temperate peatland ecosystems: The effect of
768 substrate and site, *Ecosystems*, *10*(6), 949–963, doi:10.1007/s10021-007-9064-5.

769 Muchan, K., M. Lewis, and J. Hannaford (2015), The winter storms of 2013/2014 in the UK: hydrological responses and
770 impacts, *Weather*, *70*(2), 55–61, doi:10.1002/wea.2469.

771 Musgrave, H., and A. Binley (2011), Revealing the temporal dynamics of subsurface temperature in a wetland using time-
772 lapse geophysics, *J. Hydrol.*, *396*(3-4), 258–266.

773 Newell, A. J., J. P. R. Sorensen, J. E. Chambers, P. B. Wilkinson, S. Uhlemann, C. Roberts, D. C. Gooddy, C. H. Vane, and A.
774 Binley (2015), Fluvial response to Late Pleistocene and Holocene environmental change in a Thames chalkland
775 headwater: the Lambourn of southern England, *Proc. Geol. Assoc.*, *126*(6), 683–697,
776 doi:10.1016/j.pgeola.2015.08.008.

777 Olayinka, A., and U. Yaramanci (2000), Assessment of the reliability of 2D inversion of apparent resistivity data, *Geophys.*
778 *Prospect.*, *48*, 293–316.

779 Old, G. H. et al. (2014), Instream and riparian implications of weed cutting in a chalk river, *Ecol. Eng.*, *71*, 290–300,
780 doi:10.1016/j.ecoleng.2014.07.006.

781 Oldenburg, D. W., and Y. Li (1999), Estimating depth of investigation in dc resistivity and IP surveys, *GEOPHYSICS*, *64*(2),
782 403–416, doi:10.1190/1.1444545.

783 Parsekian, A. D., X. Comas, L. Slater, and P. H. Glaser (2011), Geophysical evidence for the lateral distribution of free phase
784 gas at the peat basin scale in a large northern peatland, *J. Geophys. Res.*, *116*(G3), G03008,
785 doi:10.1029/2010JG001543.

786 Phillips, S. C., R. K. Varner, S. Frolking, J. W. Munger, J. L. Bubier, S. C. Wofsy, and P. M. Crill (2010), Interannual, seasonal,
787 and diel variation in soil respiration relative to ecosystem respiration at a wetland to upland slope at Harvard Forest,
788 *J. Geophys. Res.*, *115*(G2), 1–18, doi:10.1029/2008JG000858.

789 Picard, C. R., L. H. Fraser, and D. Steer (2005), The interacting effects of temperature and plant community type on nutrient
790 removal in wetland microcosms, *Bioresour. Technol.*, *96*(9), 1039–1047, doi:10.1016/j.biortech.2004.09.007.

791 Ponziani, M., E. C. Slob, H. Vanhala, and D. J. M. Ngan-Tillard (2012), Influence of physical and chemical properties on the
792 low-frequency complex conductivity of peat, in *Near Surface Geophysics*, vol. 10, pp. 491–501.

793 Price, J. S. (2003), Role and character of seasonal peat soil deformation on the hydrology of undisturbed and cutover
794 peatlands, *Water Resour. Res.*, *39*(9), doi:10.1029/2002WR001302.

795 Price, J. S., and S. M. Schlotzhauer (1999), Importance of shrinkage and compression in determining water storage changes
796 in peat: the case of a mined peatland, *Hydrol. Process.*, *13*(16), 2591–2601, doi:10.1002/(SICI)1099-
797 1085(199911)13:16<2591::AID-HYP933>3.0.CO;2-E.

798 Querner, E. P., P. C. Jansen, J. J. H. van den Akker, and C. Kwakernaak (2012), Analysing water level strategies to reduce soil
799 subsidence in Dutch peat meadows, *J. Hydrol.*, *446-447*, 59–69, doi:10.1016/j.jhydrol.2012.04.029.

800 Reeve, a. S., D. I. Siegel, and P. H. Glaser (2000), Simulating vertical flow in large peatlands, *J. Hydrol.*, *227*(1-4), 207–217,
801 doi:10.1016/S0022-1694(99)00183-3.

802 Reeve, A. S., R. Evensen, P. H. Glaser, D. I. Siegel, and D. Rosenberry (2006), Flow path oscillations in transient ground-
803 water simulations of large peatland systems, *J. Hydrol.*, *316*(1-4), 313–324, doi:10.1016/j.jhydrol.2005.05.005.

804 Rein, A., R. Hoffmann, and P. Dietrich (2004), Influence of natural time-dependent variations of electrical conductivity on
805 DC resistivity measurements, *J. Hydrol.*, *285*(1-4), 215–232, doi:10.1016/j.jhydrol.2003.08.015.

806 Silvola, J., J. Alm, U. Ahlholm, H. Nykänen, and P. J. Martikainen (1996), The contribution of plant roots to CO2 fluxes from
807 organic soils, *Biol. Fertil. Soils*, *23*(2), 126–131, doi:10.1007/s003740050149.

808 Slater, L., X. Comas, D. Ntarlagiannis, and M. R. Moulik (2007), Resistivity-based monitoring of biogenic gases in peat soils,
809 *Water Resour. Res.*, *43*(10), 1–13, doi:10.1029/2007WR006090.

810 Sorensen, J. P. R., and A. S. Butcher (2011), Water level monitoring pressure transducers : a need for industry-wide
811 standards, *Ground Water Monit. Remediat.*, *31*, 56–62, doi:10.1111/j1745–6592.2011.01346.x.

812 Sundh, I., M. Nilsson, G. Granberg, and B. H. Svensson (1994), Depth distribution of microbial production and oxidation of
813 methane in northern boreal peatlands, *Microb. Ecol.*, *27*(3), 253–265, doi:10.1007/BF00182409.

814 Szalai, S., A. Koppán, and L. Szarka (2008), Effect of positional inaccuracies on multielectrode results, *Acta Geod. Geophys.*
815 *Hungarica*, *43*(1), 33–42, doi:10.1556/AGeod.43.2008.1.3.

816 Theriot, J. M., J. L. Conkle, S. Reza Pezeshki, R. D. DeLaune, and J. R. White (2013), Will hydrologic restoration of Mississippi
817 River riparian wetlands improve their critical biogeochemical functions?, *Ecol. Eng.*, *60*, 192–198,
818 doi:10.1016/j.ecoleng.2013.07.021.

819 Tsourlos, P. I., J. E. Szymanski, and G. N. Tsokas (1999), The effect of terrain topography on commonly used resistivity
820 arrays, *Geophysics*, *64*(5), 1357–1363, doi:10.1190/1.1444640.

821 Uhlemann, S., P. Wilkinson, J. Chambers, H. Maurer, A. Merritt, D. Gunn, and P. Meldrum (2015), Interpolation of landslide
822 movements to improve the accuracy of 4D geoelectrical monitoring, *J. Appl. Geophys.*, submitted.

823 Uhlemann, S. S., J. P. R. Sorensen, J. E. Chambers, P. B. Wilkinson, and D. C. Gooddy (2014), Geoelectrical Monitoring of
824 Complex Hydrological Processes in a Riparian Wetland, in *Near Surface Geoscience*, pp. 14–18, Athens.

825 USDA (2007), *The PLANTS Database*, National Plant Data Center, Baton Rouge, http://plants.usda.gov.

826 Wagner, F. M., M. Möller, C. Schmidt-Hattenberger, T. Kempka, and H. Maurer (2013), Monitoring freshwater salinization
827 in analog transport models by time-lapse electrical resistivity tomography, *J. Appl. Geophys.*, *89*, 84–95,
828 doi:10.1016/j.jappgeo.2012.11.013.

829 Ward, W. O. C., P. B. Wilkinson, J. E. Chambers, L. S. Oxby, and L. Bai (2014), Distribution-based fuzzy clustering of electrical
830 resistivity tomography images for interface detection, *Geophys. J. Int.*, 1–12, doi:10.1093/gji/ggu006.

831 Watson, A., K. D. Stephen, D. B. Nedwell, and J. R. M. Arah (1997), Oxidation of methane in peat: Kinetics of CH4 and O2
832 removal and the role of plant roots, *Soil Biol. Biochem.*, *29*(8), 1257–1267, doi:10.1016/S0038-0717(97)00016-3.

833 Wilkinson, P. B., J. E. Chambers, P. I. Meldrum, D. a. Gunn, R. D. Ogilvy, and O. Kuras (2010), Predicting the movements of
834 permanently installed electrodes on an active landslide using time-lapse geoelectrical resistivity data only, *Geophys.*
835 *J. Int.*, *183*(2), 543–556.

836 Wilkinson, P. B., S. Uhlemann, J. E. Chambers, P. I. Meldrum, and M. H. Loke (2015), Development and testing of
837 displacement inversion to track electrode movements on 3-D electrical resistivity tomography monitoring grids,
838 *Geophys. J. Int.*, *200*(3), 1566–1581, doi:10.1093/gji/ggu483.

839 Yi, M.-J., J.-H. Kim, and S.-H. Chung (2003), Enhancing the resolving power of least-squares inversion with active constraint
840 balancing, *Geophysics*, *68*(3), 931, doi:10.1190/1.1581045.

841